Rapid Communications

Large-scale interlayer rotations and Te grain boundaries in $(Bi, Sb)_2Te_3$ thin films

Danielle Reifsnyder Hickey,[1,*] Ryan J. Wu,[1] Joon Sue Lee,[2,3] Javad G. Azadani,[4] Roberto Grassi,[4] Mahendra DC,[5] Jian-Ping Wang,[4] Tony Low,[4] Nitin Samarth,[2,†] and K. Andre Mkhoyan[1,‡]

[1]*Department of Chemical Engineering and Materials Science, University of Minnesota, Minneapolis, Minnesota 55455, USA*
[2]*Department of Physics and Materials Research Institute, The Pennsylvania State University, University Park, Pennsylvania 16802, USA*
[3]*California NanoSystems Institute, University of California, Santa Barbara, California 93106, USA*
[4]*Department of Electrical and Computer Engineering, University of Minnesota, Minneapolis, Minnesota 55455, USA*
[5]*School of Physics and Astronomy, University of Minnesota, Minneapolis, Minnesota 55455, USA*

(Received 27 July 2019; published 15 January 2020)

We report the observation of two distinct large-scale defects in $(Bi, Sb)_2Te_3$ topological insulator (TI) thin films grown by molecular beam epitaxy. Small-angle rotations are detected between quintuple layers of the TI film, extending throughout a grain and beyond, and nm-sized Te formations are discovered that extend along grain boundaries. Density functional theory calculations suggest that the rotational defects can affect the local band structure of the film while preserving spin-momentum locking in the Dirac bands, and that the Te nanostructures at grain boundaries can result in wider-band-gap regions between the grains.

DOI: 10.1103/PhysRevMaterials.4.011201

Thin-film topological insulators (TIs) are exciting candidates for integration into next-generation memory and logic devices because of their potential for efficient, low-energy-consumption switching of magnetization [1,2]. The bismuth chalcogenides—specifically Bi_2Se_3, Bi_2Te_3, and $(Bi, Sb)_2Te_3$—have already demonstrated topologically protected surface states that can generate spin-transfer torque, current-induced spin polarization, and ferromagnetic resonance-driven room-temperature spin pumping [2–6]. They also offer efficient spin-to-charge conversion because of their large spin-orbit coupling and spin-momentum locking of surface states [7,8]. Additionally, their tetradymite crystal structure is two dimensionally (2D) layered [9,10] and can grow without the stringent requirements of lattice parameter matching [11–16].

The quality of these thin-film bismuth chalcogenide TIs still lags behind that of epitaxially grown semiconductors [8]. Understanding and controlling defects and grain boundaries [17–20] within the films is one of the limitations for achieving breakthrough device performances. Interestingly, very little is known about defects that are unique to thin films. Here, we report direct identification and characterization of two distinct large-scale defects in $(Bi, Sb)_2Te_3$ thin films: (i) small-angle rotations between the TI layers and (ii) nm-wide Te formations extending along the grain boundaries.

The films of $(Bi, Sb)_2Te_3$ were grown by molecular beam epitaxy (MBE) onto exfoliated *h*-BN specifically for this plan-view transmission electron microscopy (TEM) study. We focused our study on films that are not completely coalesced, as they enable direct analysis of grains and grain boundaries. The TI films were approximately two-to-three unit cells thick in the *c*-direction. The film morphology is shown in high-angle annular dark-field scanning TEM (HAADF-STEM) image in Fig. 1(a), along with elemental maps (for cross-sectional analysis, see SM Fig. S1 [21]). The films show many grain-level irregular and regular triangular terraces [Figs. 1(b) and 1(c)], all of which contribute to thickness variations in the film. The HAADF-STEM intensity [Fig. 1(c)] shows that these films can have not only full- but also fractional-unit-cell thickness and, therefore, terracing at grain boundaries.

Low-magnification conventional TEM (CTEM) images obtained from these films show quasiperiodic Moiré patterns that provide clues about large-scale defects in the film [Figs. 2(a) and 2(b)] that are not detectable *via* surface techniques. Entire grains exhibit these features, and in some cases, they persist across grain boundaries where islands have coalesced. Rotations within the TI layers can give rise to these patterns, which can be reproduced by CTEM image simulations when the two-component $(Bi, Sb)_2Te_3/h$-BN heterostructure is divided into a three-layer system: the *h*-BN substrate, and the TI film divided into two independent layers, with one TI layer rotated relative to the other. The patterns observed in CTEM images are identified from a series of simulated images using MULTISLICE code [22] by varying the angles for the layer rotations (see Supplemental Material (SM) Figs. S2, S3 [21]). It should be noted that such quasiperiodic Moiré patterns cannot be reproduced when the heterostructure is treated as only the two-layer system (TI film and *h*-BN substrate; see SM Fig. S2 [21]) [23,24]. Only rotation between the two TI layers gives rise to these large-period, quasiperiodic features.

Figure 2(b) shows a comparison of experimental and simulated images for the two distinct regions of the film: region R1 with large, wavy, quasiperiodic features with a period of tens of nanometers corresponding to 0.5° rotation between TI

*Present address: Department of Materials Science, The Penn State University, University Park, Pennsylvania 16802, USA; drh283@psu.edu
†Corresponding author: nsamarth@psu.edu
‡Corresponding author: mkhoyan@umn.edu

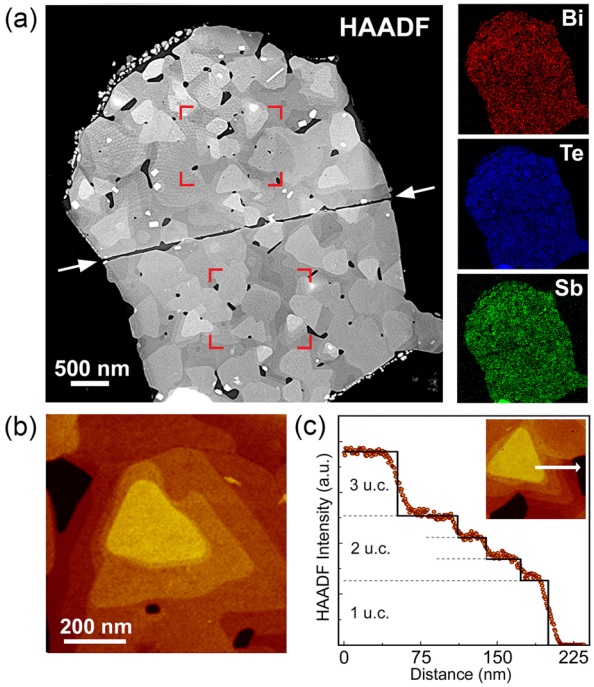

FIG. 1. (a) HAADF-STEM plan-view image of the $(Bi, Sb)_2Te_3$ TI film grown on an *h*-BN flake, with accompanying elemental EDX maps. (b) HAADF-STEM image of an irregular triangular feature in the TI film. (c) HAADF-STEM intensity across the region marked by arrow in the inset image of a regular triangular terrace. Black lines are a guide to the eye, showing the unit cell (u.c.) and fractional steps.

layers, and featureless region R2 that has no Moiré contrast. Region R3, which is a subcategory of R1, exhibits smaller, quasiperiodic features with a period of ∼5 nm corresponding to 2° rotation between TI layers. Additionally, transitions from small to much larger periodicities are visible in some areas. Although they are striking in the plan-view images shown here, these small-angle rotations between layers are very challenging to identify in cross-sectional ADF-STEM images [25].

When two TI layers are rotated 60° relative to each other, they form a basal twin [26]. A small interlayer rotation around 0° and the 60° twin result in similar Moiré patterns (e.g., 2° and 62° resemble each other (see SM Figs. S2(a), S3(a) [21])), suggesting that some of the patterns seen in CTEM images could be from small-angle rotations around a basal twin. Image simulations also show that the Moiré patterns disappear near 30° (see SM Fig. S3(b) [21]), but the 30° rotation can be identified by diffraction patterns. Figure 2(c) shows that the grain with featureless contrast in region R2 is in fact a case of ∼30° rotation between the TI layers.

To evaluate the potential impact of these rotations between TI layers on the basic properties of the film, density functional theory (DFT) calculations were performed for simpler, nonalloyed, 3-QL-thick Bi_2Te_3 and Sb_2Te_3 films (Fig. 3). The results predict that (i) rotations between layers, including basal twins, can result in a reduction of the bulk band gap, which was also observed by Schouteden *et al.* [24], and (ii) preservation of the important 90° spin-momentum locking in

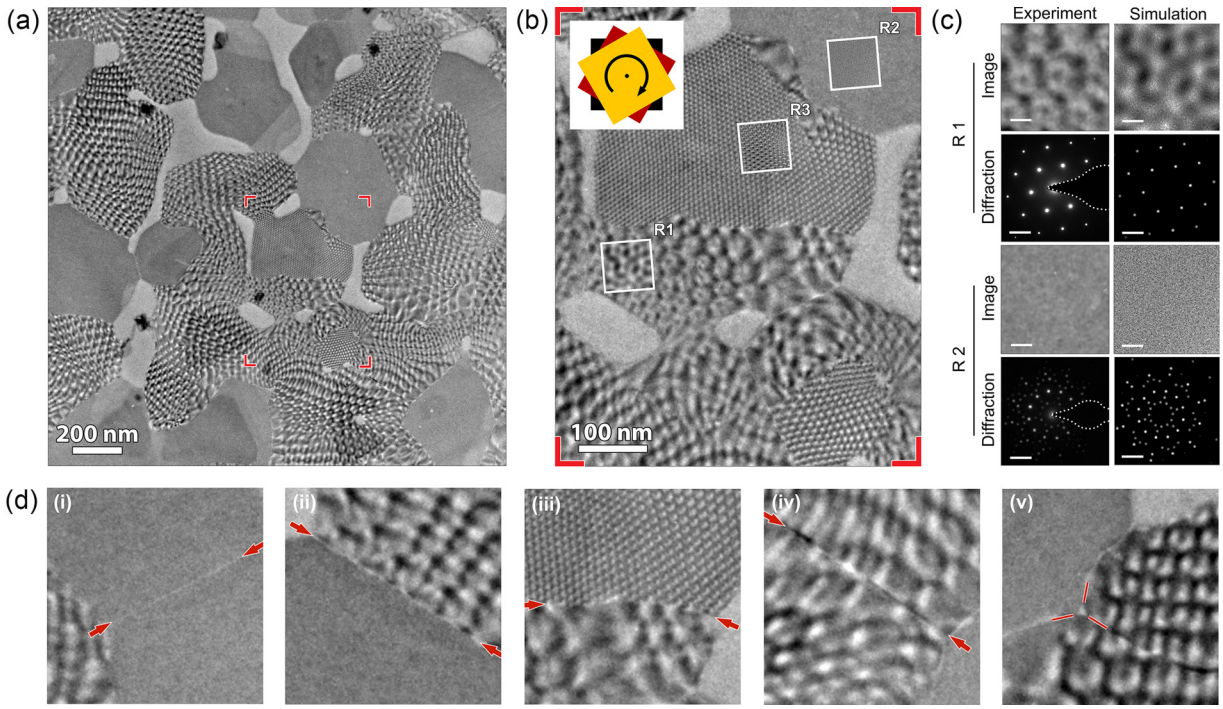

FIG. 2. (a) Low-magnification CTEM image of the $(Bi, Sb)_2Te_3/h$-BN heterostructure showing large-scale Moiré patterns. (b) Magnified section of the image in (a) (indicated by red marks) showing three different regions, with *Multislice* simulated images overlaid: region R1 with 0.5°, region R2 with ∼30°, and region R3 with 2° rotations between TI layers. Inset, a three-layer TI/TI/h-BN model with relative rotations between the layers (black = *h*-BN, maroon = TI-1, and yellow = TI-2). (c) Experimental and simulated images and diffraction patterns for regions R1 and R2. (d) Examples of grain boundaries in the film (indicated by red arrows) and, in some cases, Moiré patterns crossing the grain boundary.

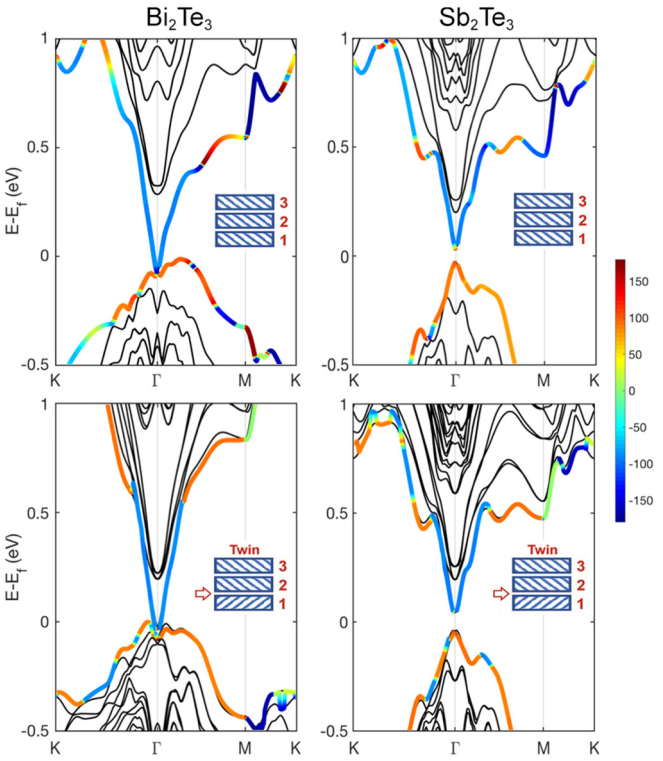

FIG. 3. DFT-calculated band structures of pristine (top) and basal twinned (bottom), i.e., rotated 60°, three-QL Bi_2Te_3 and Sb_2Te_3. The angle between wave vector k and spin s of the electron located in the top surface QL is identified by color map. The location of the basal twin is indicated in the inset schematic.

the Dirac bands in the vicinity of the Γ point can be expected (see also SM Figs. S4 [21]).

Some grain boundaries in these $(Bi, Sb)_2Te_3$ thin films contain ribbon-like and wire-like nanoregions of hexagonal $P3_121$ Te (Fig. 4, also SM Fig. S5 [21]) [27–29]. Atomic-

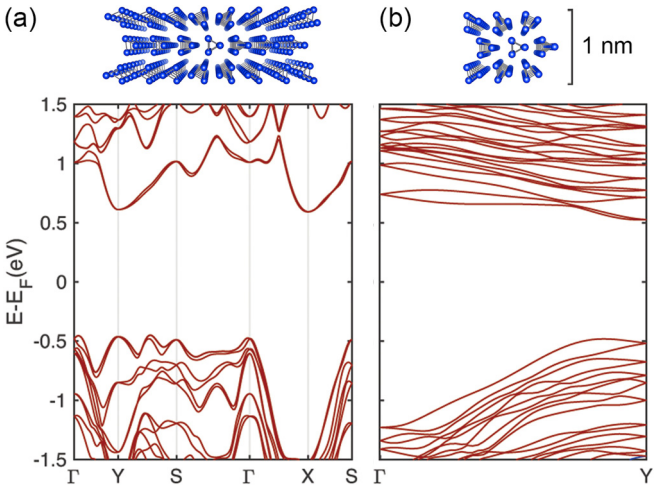

FIG. 5. DFT-calculated band structures of Te nanoregions: (a) ribbon-like and (b) wire-like. The atomic configurations of the relaxed structures used in calculations are shown above.

resolution HAADF-STEM images show the characteristic van der Waals-bonded chiral 1D structure of Te. The EDX analysis confirms the composition (with <15 at. % Bi and Sb in the region). To the best of our knowledge, this is the first observation of the formation of Te nanostructures at grain boundaries. Interestingly, TI regions adjacent to these grain boundaries show Te depletion in the $(Bi, Sb)_2Te_3$ film [Fig. 4(b)], suggesting a possible migration of Te from neighboring grains. These Te nanoregions in some places are 20–100 nm long, running along a large portion of the grain boundary [Fig. 4(d)].

Using DFT, we investigated the basic electronic properties of such Te nanoregions. The electronic band structures were calculated for three-triangle-wide Te nanostructures with a geometry similar to those observed in HAADF-STEM images [Fig. 4(d)], but without the host $(Bi, Sb)_2Te_3$. The structural relaxation resulted in 1.1-nm-wide Te ribbon-like and

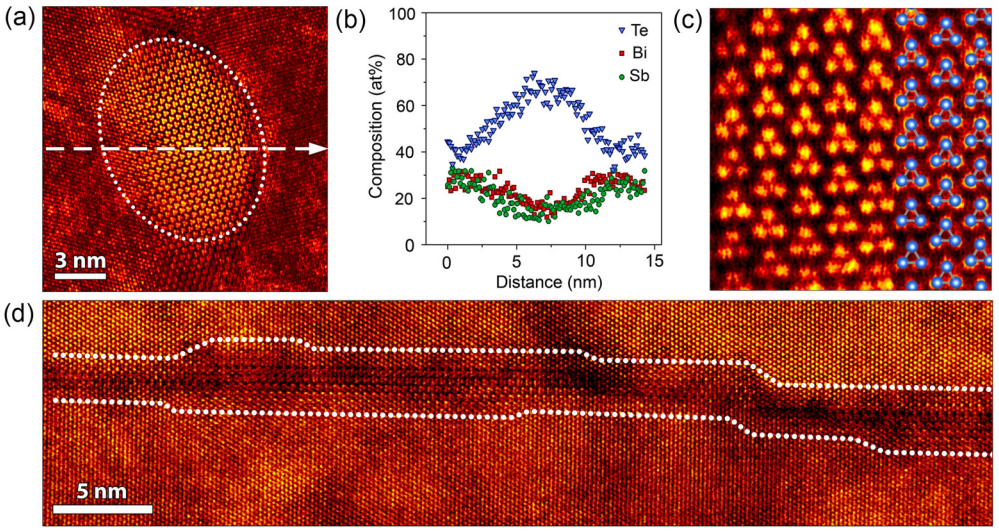

FIG. 4. (a) HAADF-STEM image of a Te pocket at a grain boundary. (b) EDX line scan of the Te pocket shown in (a), obtained along the arrow. (c) Atomic-resolution HAADF-STEM image showing the structure of the Te with a ball-and-stick model overlay. (d) Image of a section of a long Te nanoregion at a grain boundary.

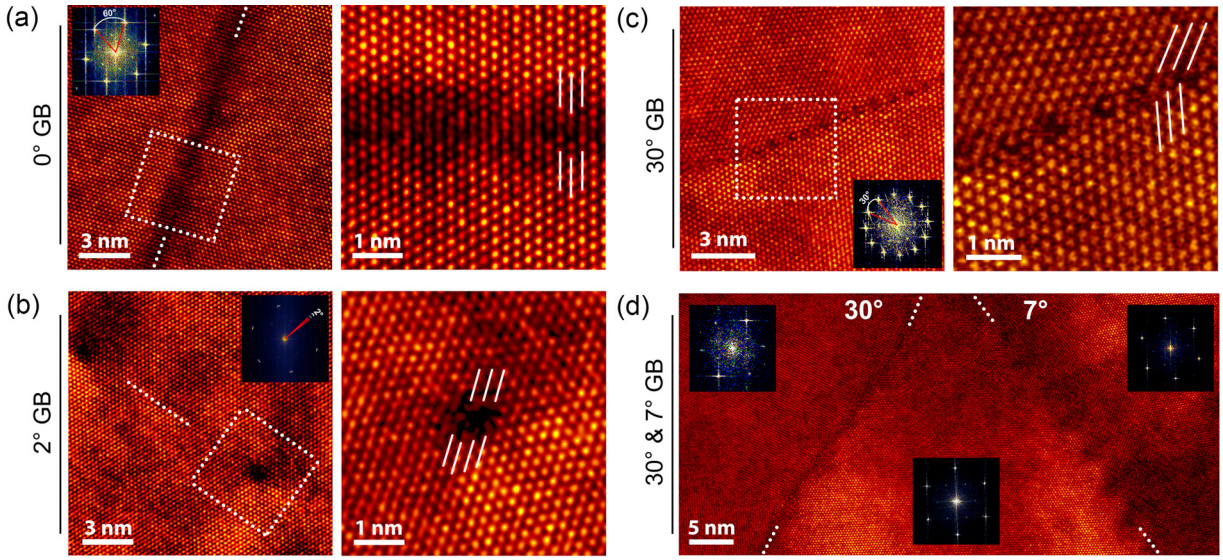

FIG. 6. Low- and high-magnification HAADF-STEM images of a grain boundary with (a) 0° (or 60°) misorientation, (b) 2° misorientation with dislocations, and (c) 30° misorientation, along with FFTs. Dashed boxes indicate the regions shown at higher magnification. (d) Image of three grains connected by 30° and 7° grain boundaries with corresponding single-grain FFTs.

1.0×1.3 nm wire-like structures. The electronic band structures, calculated with the HSE06 hybrid functional, which is known for its improved band gap prediction capability [30], show dramatic changes in the band structure due to quantization (Fig. 5) with considerably increased band gap: ${E_g}^{r\text{-}l} = 1.04$ eV for ribbon-like and ${E_g}^{w\text{-}l} = 1.01$ eV for wire-like Te, compared to $E_g = 0.35$ eV for the bulk Te [31]. Due to very high energies of core-level s and p orbitals (>4 keV), currently available electron energy-loss spectrometers cannot probe the Te K or $L_{2,3}$ edges necessary to measure the predicted band structures and associated density of states in these nanoregions (accessible $N_{4,5}$ and $M_{4,5}$ edges lack the fine structure [32]).

Not all grain boundaries in these films contain Te nanostructures. A considerable fraction of the grains coalesce with 0° (or 60°), 2°, 7°, and 30° misorientations without diffusing out Te (Fig. 6). The low-angle (2° and 7°) grain boundaries consist of an array of dislocations [Figs. 6(b) and 6(d)], similar to those observed in bulk Bi_2Se_3 [20], which are predicted to be semimetallic [33]. Our observations suggest that when correlation between film growth conditions and resulting grain boundaries is achieved, it would be possible to either avoid formation of the Te nanostructures at the boundaries, or produce films with predominantly Te ribbon-like walls between the grains with unexpected properties.

In conclusion, we have shown that two different large-scale defects are present in $(Bi, Sb)_2Te_3$ thin-film TIs grown by MBE. These include small-angle rotations between quintuple layers that in some cases extend beyond a single grain, as well as the formation of nm-sized structures of Te at grain boundaries, with regions extending to 10s of nm in length. DFT calculations predict that rotational defects can affect the local band structure of the film, while preserving spin-momentum locking in Dirac bands, and that the Te nanoregions can be semiconducting with band gaps as large as 1 eV. Advancements in electron-energy-loss spectrosctopy (EELS) instrumentation will allow direct measurements of the electronic structures of these Te nanoregions.

This study suggests that when the growth conditions are identified for the systematic production of TI thin films with rotated layers or with 1D chiral Te walls at grain boundaries, it will open up possibilities to discover physical phenomena in TI thin films, as has been the case with other 2D materials [34–37], based on Moiré patterns, symmetry breaking, and the engineering of types of grain boundaries.

This work was supported by C-SPIN, one of six STARnet program research centers and SMART, one of seven centers of nCORE, a Semiconductor Research Corporation program, sponsored by NIST. This work utilized the College of Science and Engineering Characterization Facility, University of Minnesota (UMN), supported in part by the NSF through the UMN MRSEC Program No. DMR-1420013.

[1] Y. Ando, J. Phys. Soc. Jpn. **82**, 102001 (2013).
[2] A. R. Mellnik, J. S. Lee, A. Richardella, J. L. Grab, P. J. Mintun, M. H. Fischer, A. Vaezi, A. Manchon, E.-A. Kim, N. Samarth, and D. C. Ralph, Nature (London) **511**, 449 (2014).
[3] H. Zhang, C.-X. Liu, X. L. Qi, X. Dai, Z. Fang, and S. C. Zhang, Nat. Phys. **5**, 438 (2009).
[4] Y. L. Chen, J. G. Analytis, J. H. Chu, Z. K. Liu, S. K. Mo, X. L. Qi, H. J. Zhang, D. H. Lu, X. Dai, Z. Fang, S. C. Zhang, I. R. Fisher, Z. Hussain, and Z.-X. Shen, Science **325**, 178 (2009).

[5] J. S. Lee, A. Richardella, D. R. Hickey, K. A. Mkhoyan, and N. Samarth, Phys. Rev. B **92**, 155312 (2015).

[6] H. Wang, J. Kally, J. S. Lee, T. Liu, H. Chang, D. R. Hickey, K. A. Mkhoyan, M. Wu, A. Richardella, and N. Samarth, Phys. Rev. Lett. **117**, 076601 (2016).

[7] M. Z. Hasan and C. L. Kane, Rev. Mod. Phys. **82**, 3045 (2010).

[8] J. J. Heremans, R. J. Cava, and N. Samarth, Nat. Rev. Mater. **2**, 17049 (2017).

[9] S. Xu, Y. Han, X. Chen, Z. Wu, L. Wang, T. Han, W. Ye, H. Lu, G. Long, Y. Wu, J. Lin, Y. Cai, K. M. Ho, Y. He, and N. Wang, Nano Lett. **15**, 2645 (2015).

[10] J. Y. Park, G.-H. Lee, J. Jo, A. K. Cheng, H. Yoon, K. Watanabe, T. Taniguchi, M. Kim, P. Kim, and G.-C. Yi, 2D Mater. **3**, 035029 (2016).

[11] M. I. Bakti Utama, Q. Zhang, J. Zhang, Y. Yuan, F. J. Belarre, J. Arbiol, and Q. Xiong, Nanoscale **5**, 3570 (2013).

[12] Y. C. Lin, N. Lu, N. Perea-Lopez, J. Li, Z. Lin, X. Peng, C. H. Lee, C. Sun, L. Calderin, P. N. Browning, M. S. Bresnehan, M. J. Kim, T. S. Mayer, M. Terrones, and J. A. Robinson, ACS Nano **8**, 3715 (2014).

[13] C.-L. Song, Y. L. Wang, Y.-P. Jiang, Y. Zhang, C. Z. Chang, L. Wang, K. He, X. Chen, J.-F. Jia, Y. Wang, Z. Fang, X. Dai, X.-C. Xie, X. L. Qi, S.-C. Zhang, Q. K. Xue, and X. Ma, Appl. Phys. Lett. **97**, 143118 (2010).

[14] S. Rajput, Y. Y. Li, M. Weinert, and L. Li, ACS Nano **10**, 8450 (2016).

[15] L. He, X. Kou, and K. L. Wang, Phys. Status Solidi RRL **7**, 50 (2013).

[16] A. Richardella, A. Kandala, J. S. Lee, and N. Samarth, APL Mater. **3**, 083303 (2015).

[17] L. Seixas, L. B. Abdalla, T. M. Schmidt, A. Fazzio, and R. H. Miwa, J. Appl. Phys. **113**, 023705 (2013).

[18] K. C. Kim, J. Lee, B. K. Kim, W. Y. Choi, H. J. Chang, S. O. Won, B. Kwon, S. K. Kim, D. B. Hyun, H. J. Kim, H. C. Koo, J. H. Choi, D. I. Kim, J. S. Kim, and S. H. Baek, Nat. Commun. **7**, 12449 (2016).

[19] Y. Liu, Y. Y. Li, D. Gilks, V. K. Lazarov, M. Weinert, and L. Li, Phys. Rev. Lett. **110**, 252001 (2013).

[20] Y. Liu, Y. Y. Li, S. Rajput, D. Gilks, L. Lari, P. L. Galindo, M. Weinert, V. K. Lazarov, and L. Li, Nat. Phys. **10**, 294 (2014).

[21] See Supplemental Material at http://link.aps.org/supplemental/10.1103/PhysRevMaterials.4.011201 for a description of experimental and computational parameters and methods, data analysis, supplementary figures, and Refs. [22,38–45].

[22] E. J. Kirkland, *Advanced Computing in Electron Microscopy*, 2nd ed. (Springer, New York, 2010).

[23] Y. Liao, W. Cao, J. W. Connell, Z. Chen, and Y. Lin, Sci. Rep. **6**, 26084 (2016).

[24] K. Schouteden, Z. Li, T. Chen, F. Song, B. Partoens, C. Van Haesendonck, and K. Park, Sci. Rep. **6**, 20278 (2016).

[25] S. E. Maccagnano-Zacher, K. A. Mkhoyan, E. J. Kirkland, and J. Silcox, Ultramicroscopy **108**, 718 (2008).

[26] D. Reifsnyder Hickey, J. G. Azadani, A. R. Richardella, J. C. Kally, J. S. Lee, H. Chang, T. Liu, M. Wu, N. Samarth, T. Low, and K. A. Mkhoyan, Phys. Rev. Mater. **3**, 061201(R) (2019).

[27] *ASM Handbook, Vol. 3, Alloy Phase Diagrams*, edited by H. Okamoto, M. E. Schlesinger, and E. M. Mueller (ASM International, Materials Park, OH, 2016).

[28] L. Cheng, Z. G. Chen, L. Yang, G. Han, H. Y. Xu, G. J. Snyder, G. Q. Lu, and J. Zou, J. Phys. Chem. C **117**, 12458 (2013).

[29] Y. Zhao, M. de la Mata, R. L. J. Qiu, J. Zhang, X. Wen, C. Magen, X. P. A. Gao, J. Arbiol, and Q. Xiong, Nano Res. **7**, 1243 (2014).

[30] J. Heyd, J. E. Peralta, G. E. Scuseria, and R. L. Martin, J. Chem. Phys. **123**, 174101 (2005).

[31] H. Peng, N. Kioussis, and G. J. Snyder, Phys. Rev. B **89**, 195206 (2014).

[32] C. C. Ahn and O. L. Krivanek, *EELS Atlas: A Reference Collection of Electron Energy Loss Spectra Covering all Stable Elements* (Gatan, Inc., Warrendale, PA, 1983).

[33] R. J. Slager, V. Juricic, V. Lahtinen, and J. Zaanen, Phys. Rev. B **93**, 245406 (2016).

[34] K. L. Seyler, P. Rivera, H. Yu, N. P. Wilson, E. L. Ray, D. G. Mandrus, J. Yan, W. Yao, and X. Xu, Nature (London) **567**, 66 (2019).

[35] K. Tran, G. Moody, F. Wu, X. Lu, J. Choi, K. Kim, A. Rai, D. A. Sanchez, J. Quan, A. Singh, J. Embley, A. Zepeda, M. Campbell, T. Autry, T. Taniguchi, K. Watanabe, N. Lu, S. K. Banerjee, K. L. Silverman, S. Kim, E. Tutuc, L. Yang, A. H. MacDonald, and X. Li, Nature (London) **567**, 71 (2019).

[36] C. Jin, E. C. Regan, A. Yan, M. I. B. Utama, D. Wang, S. Zhao, Y. Qin, S. Yang, Z. Zheng, S. Shi, K. Watanabe, T. Taniguchi, S. Tongay, A. Zettl, and F. Wang, Nature (London) **567**, 76 (2019).

[37] E. M. Alexeev, D. A. Ruiz-Tijerina, M. Danovich, M. J. Hamer, D. J. Terry, P. K. Nayak, S. Ahn, S. Pak, J. Lee, J. I. Sohn, M. R. Molas, M. Koperski, K. Watanabe, T. Taniguchi, K. S. Novoselov, R. V. Gorbachev, H. S. Shin, V. I. Falko, and A. I. Tartakovskii, Nature (London) **567**, 81 (2019).

[38] J. M. Cowley and A. F. Moodie, Acta Crystallogr. **10**, 609 (1957).

[39] M. M. Stasova and N. K. Abrikosov, Izv. Akad. Nauk SSSR, Neorg. Mater. **6**, 1090 (1970).

[40] *Semiconductors · Group IV Elements, IV-IV and III-V Compounds. Part A - Lattice Properties*, edited by O. Madelung, U. Rössler, and M. Schulz (Springer-Verlag, Berlin, 2001).

[41] M. L. Odlyzko and K. A. Mkhoyan, Microsc. Microanal. **18**, 558 (2012).

[42] B.-L. Huang and M. Kaviany, Phys. Rev. B **77**, 125209 (2008).

[43] G. Kresse and J. Furthmüller, Phys. Rev. B **54**, 11169 (1996).

[44] J. P. Perdew, K. Burke, and M. Ernzerhof, Phys. Rev. Lett. **77**, 3865 (1996).

[45] P. E. Blöchl, Phys. Rev. B **50**, 17953 (1994).